Shape optimization of metallic yielding devices for passive mitigation of seismic energy

Kazem Ghabraie[a], Ricky Chan[b,*], Xiaodong Huang[b], Yi Min Xie[b]

[a]*Faculty of Engineering and Surveying, University of Southern Queensland, Toowoomba Qld 4350, Australia*
[b]*School of Civil, Environmental and Chemical Engineering, RMIT University, GPO Box 2476, Melbourne VIC 3001, Australia*

Abstract

Bi-directional Evolutionary Structural Optimization (BESO) is a well established topology optimization technique. This method is used in this paper to optimize the shape of a passive energy dissipater designed for earthquake risk mitigation. A previously proposed shape design of a steel slit damper (SSD) device is taken as the initial design and its shape is optimized using a slightly modified BESO algorithm. Some restrictions are imposed to maintain simplicity and to reduce fabrication cost. The optimized shape shows increased energy dissipation capacity and even stress distribution. Experimental verification has been carried out and proved that the optimized shape is more resistant to low-cycle fatigue.

Keywords: Shape optimization, Energy dissipation, Bi-directional Evolutionary Structural Optimization, Metallic damper, Cyclic tests, Earthquake resistant structure

*Corresponding author
Email addresses: kazem.ghabraie@usq.edu.au (Kazem Ghabraie), ricky.chan@rmit.edu.au (Ricky Chan), xiaodong.huang@rmit.edu.au (Xiaodong Huang), mike.xie@rmit.edu.au (Yi Min Xie)

1. Introduction

In the last two decades development of energy dissipation devices for mitigation of wind and earthquake has flourished. Various types of passive, semi-active and active devices have been proposed, tested and implemented [1]. With this technology, a large portion of input energy from wind or earthquake excitations is dissipated by designated devices. As a result, structural responses are suppressed, and major structural elements can be protected from damage. Particularly in earthquake applications, metallic devices which utilize yield deformation of metals remain among the most popular types selected by engineers. They are reliable, inexpensive to fabricate, easy to install and maintain. Metallic devices can be classified into flexural types, such as hourglass shape ADAS [2], triangular shape TADAS [3]; shear types such as YSPD [4] and axial types, such as the Buckling Retrained Brace [5]. Devices are mainly designed to be incorporated into lateral-load-resisting system in structural frames, but some are developed to be installed between beam and columns [6].

Design of metallic devices requires several desirable engineering characteristics:

1. possessing sufficient elastic strength and stiffness such that device is not excited to inelastic region under service loads;
2. having stable and large energy dissipative capability; and
3. having reasonable resistance against low-cycle fatigue.

With respect to low-cycle fatigue, current design standard in the United States requires devices to undergo five fully reversed cycles at maximum earthquake device displacement (ASCE/SEI 7-05). Generally, in order to increase the resistance to low-cycle fatigue, stress concentration has to be avoided.

Along with the revolutionary improvement of digital computers in recent decades, computational methods and numerical techniques have established their place as invaluable engineering tools. Among these, numerical optimization methods have attracted a great number of researchers and have been improved a lot. Particularly, the state-of-the-art shape and topology optimization techniques have been applied to a range of physical problems and have been proved to yield much better results than experimental designs [8, 9]. The Evolutionary Structural Optimization (ESO) method, introduced by Xie and Steven [10] is a simple and effective topology optimization technique which can tackle shape optimization problems as well. This method iteratively improves the design domain by removing its inefficient parts. A Bi-directional version of the ESO method, called BESO, has been later proposed by Querin et al. [11, 12] and Yang et al. [13]. In BESO, besides removal of inefficient parts, the efficient parts of the design domain will be improved by adding more material next to them. Since its introduction, the BESO algorithm has been improved significantly [14]. The improved BESO algorithm has been successfully applied to non-linear problems [15, 16]. This method is also capable of optimizing both shape and topology of the designs [17].

In this paper, the BESO algorithm is modified to optimize the shape of an existing steel slit damper device design (SSD). The proposed algorithm applies some shape restrictions to the design to make the final shape easily manufacturable. An efficient device design should possess a high energy dissipation capability per unit volume. To gain this, the proposed algorithm maximizes the total plastic dissipation. It is also demonstrated that the optimum design resulted from the proposed optimization algorithm, show less stress concentration than the initial design.

In order to verify the numerical results and to address the shortcomings of the

numerical models, physical experiments are carried out. It is demonstrated that experimental outcomes support the numerical results.

2. Optimization

Chan and Albermani [18] have proposed a class of simple designs for SSD devices supported by a series of experimental test results. Fig. 1 shows the typical shape of the device. The size of the slits (w) can be controlled by varying l and b. In this paper, a new class of design is proposed by optimizing the shape of the slits in Fig. 1. To achieve this, a shape optimization algorithm based on the BESO technique is proposed and utilized here. Some restrictions are imposed to maintain the simplicity of the shape and hence reduce its fabrication costs. These restrictions are discussed in detail in Section 2.4.

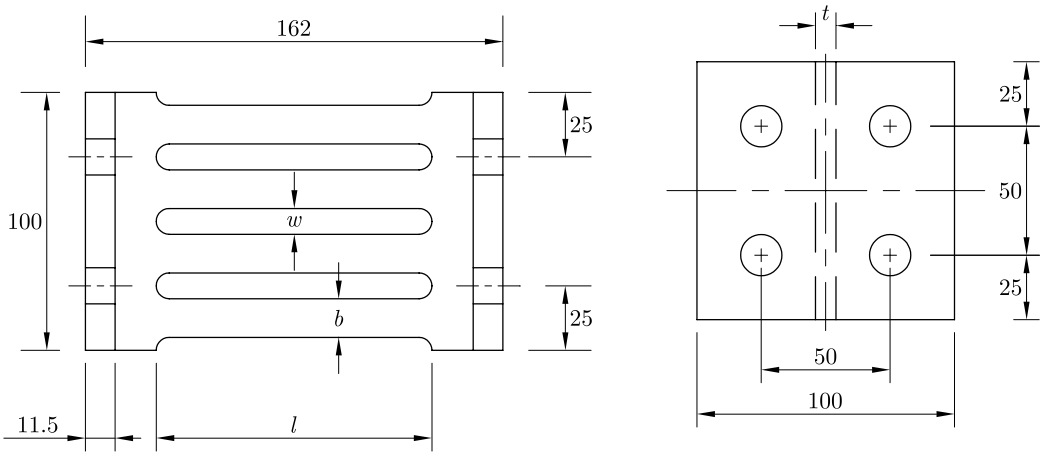

Figure 1: The SSD device design proposed by Chan and Albermani [18].

2.1. Numerical modeling

For numerical modeling, the flanges are considered solid and a plane stress rectangular mesh is used to model the web. A uniform web thickness of t = 8mm

is considered overall the design except for the elements on the far left and right sides of the domain. These elements which are in the vicinity of the flanges are modeled using thicker elements to simulate fillets (Fig. 2).

For the sake of fabrication, the holes are prevented from being too wide by setting the two strips of 15mm width on the left and right sides as non-designable elements. Fig. 2 illustrates the designable and non-designable domains.

The left side of the model is fixed and a uniform vertical displacement is applied to the right side of the model. The loading cycle consists of three steps: an upward displacement of 10mm, followed by a downward displacement of 20mm, and finally an upward displacement of 10mm up to the original location (Fig. 2). In this manner the elastic strain energy will be zero after a full cycle and the total strain energy would be equal to the total plastic dissipation.

2.2. Problem statement

To optimize the shape of the SSD, the total plastic energy dissipation is considered as the objective function which is to be maximized. In order to prevent the optimization algorithm from catching the extreme full or empty domain designs, it is necessary to include an additional constraint to restrict the amount of usable material [19]. Here we use a volume constraint which forces the algorithm to use a certain amount of material in the design domain. Alternatively, one can impose a restriction on the maximum force instead of using a volume constraint [15]. The optimization problem can be expressed as

$$\begin{aligned} \max_{x_1,x_2,\ldots,x_N} \quad & E_P \\ \text{subject to} \quad & V = \bar{V} \\ \text{and} \quad & \text{shape restrictions} \end{aligned} \tag{1}$$

where E_P is the total plastic dissipation; V and $\bar{V}$ are the actual and target volumes; x_i-s are the design variables and N is the number of elements in the design domain. Shape restrictions are fully covered in Section 2.4. In the BESO algorithm, design variables are binary values with $x = 1$ indicating the presence of material in the i-th element and $x = 0$ representing a void in the location of the i-th element.

2.3. Sensitivity analysis

To evaluate the effect of adding or removing an element during the optimization process, one needs to perform a sensitivity analysis.

Because the loading sequence consists of a full cycle, the total plastic dissipation will be equal to the total strain energy. Hence, for this case, we can write

$$E_P = E_T = \oint \mathbf{f} \cdot \mathrm{d}\mathbf{u}, \tag{2}$$

where E_T is the total strain energy; and $\mathbf{f}$ and $\mathbf{u}$ are nodal force and displacement vectors respectively. Using the trapezoidal method for numerical integration, this definition can be rewritten as

$$E_P = \lim_{n\to\infty} \left[\frac{1}{2} \sum_{i=1}^{n} \left(\mathbf{u}_i^T - \mathbf{u}_{i-1}^T \right) (\mathbf{f}_i + \mathbf{f}_{i-1}) \right]. \tag{3}$$

The shape sensitivities of the nonlinear systems have been calculated for different types of problems by Huang and Xie [16], Buhl et al. [20], Jung and Gea [21]. Here we briefly describe the sensitivity analysis of the problem (1) based on Huang and Xie [16].

To solve the non-linear equilibrium system, an iterative procedure is commonly used to eliminate the residual force. The residual force vector, $\mathbf{r}$, is defined as the difference between the external and internal force vectors. The equilibrium can thus be expressed as

$$\mathbf{r} = \mathbf{f} - \hat{\mathbf{f}} = 0. \tag{4}$$

The internal force vector $\hat{\mathbf{f}}$ is defined as

$$\hat{\mathbf{f}} = \sum_{e=1}^{N} \int_{V_e} \mathbf{C}_e^T \mathbf{B}^T \boldsymbol{\sigma} \mathrm{d}V = \sum_{e=1}^{N} \mathbf{C}_e^T \mathbf{p}_e \tag{5}$$

with $\mathbf{C}_e$ denoting the matrix that transforms the local nodal values of the e-th element to global nodal values; $\mathbf{B}$ being the matrix that transforms a change in displacement into a change in strain; and $\boldsymbol{\sigma}$ representing the local element stress vector.

In order to calculate the sensitivities of the objective function, E_P, with respect to a design variable, x, we rewrite the (3) by adding an adjoint vector $\boldsymbol{\lambda}$ multiplied by a zero function

$$E_P = \lim_{n\to\infty} \left[\frac{1}{2} \sum_{i=1}^{n} \left(\mathbf{u}_i^T - \mathbf{u}_{i-1}^T \right) (\mathbf{f}_i + \mathbf{f}_{i-1}) - \boldsymbol{\lambda}_i^T \left(\mathbf{r}_i + \mathbf{r}_{i-1} \right) \right]. \tag{6}$$

Now, differentiating (6) with respect to x, one can obtain

$$\begin{aligned} \frac{\partial E_p}{\partial x} = \lim_{n\to\infty} \Bigg[& \frac{1}{2} \sum_{i=1}^{n} \left(\mathbf{u}_i^T - \mathbf{u}_{i-1}^T \right) \left(\frac{\partial \mathbf{f}_i}{\partial x} + \frac{\partial \mathbf{f}_{i-1}}{\partial x} \right) \\ & + \frac{1}{2} \sum_{i=1}^{n} \left(\frac{\partial \mathbf{u}_i^T}{\partial x} - \frac{\partial \mathbf{u}_{i-1}^T}{\partial x} \right) (\mathbf{f}_i + \mathbf{f}_{i-1}) \\ & - \boldsymbol{\lambda}_i^T \left(\frac{\partial \mathbf{r}_i}{\partial x} + \frac{\partial \mathbf{r}_{i-1}}{\partial x} \right) \Bigg]. \end{aligned} \tag{7}$$

The system of concern is subject to a gradual change in displacement at certain nodes. At those degrees of freedom where the displacement is explicitly defined, $\frac{\partial u_j}{\partial x} = 0$. Everywhere else, $f_j = 0$. The second term in the above equation, thus, cancels out. Further, by considering (4), the above equation can be simplified to

$$\begin{aligned} \frac{\partial E_p}{\partial x} = \lim_{n\to\infty} \Bigg[& \frac{1}{2} \sum_{i=1}^{n} \left(\mathbf{u}_i^T - \mathbf{u}_{i-1}^T \right) \left(\frac{\partial \mathbf{f}_i}{\partial x} + \frac{\partial \mathbf{f}_{i-1}}{\partial x} \right) \\ & - \boldsymbol{\lambda}_i^T \left(\frac{\partial \mathbf{f}_i}{\partial x} + \frac{\partial \mathbf{f}_{i-1}}{\partial x} \right) + \boldsymbol{\lambda}_i^T \left(\frac{\partial \hat{\mathbf{f}}_i}{\partial x} + \frac{\partial \hat{\mathbf{f}}_{i-1}}{\partial x} \right) \Bigg]. \end{aligned} \tag{8}$$

To eliminate the unknown terms in (8), the adjoint equation is defined as

$$\boldsymbol{\lambda}_i = \mathbf{u}_i - \mathbf{u}_{i-1} \tag{9}$$

from which the adjoint vector is readily calculable. Now, using (9) in (8), one can get

$$\frac{\partial E_p}{\partial x} = \lim_{n\to\infty}\left[\frac{1}{2}\sum_{i=1}^{n}\left(\mathbf{u}_i^T - \mathbf{u}_{i-1}^T\right)\left(\frac{\partial \hat{\mathbf{f}}_i}{\partial x} + \frac{\partial \hat{\mathbf{f}}_{i-1}}{\partial x}\right)\right]. \tag{10}$$

The validity of this sensitivity analysis is demonstrated through a simple analytical problem by Huang and Xie [16].

Using a linear approximation, one can write

$$\frac{\partial E_P}{\partial x} \approx \frac{\Delta E_P}{\Delta x} \tag{11}$$

and

$$\frac{\partial \hat{\mathbf{f}}}{\partial x} \approx \frac{\Delta \hat{\mathbf{f}}}{\Delta x}. \tag{12}$$

Now using (12) and (11) in (10), the change in the energy dissipation due to a change in a design variable can be approximated as

$$\Delta E_p \approx \lim_{n\to\infty}\left[\frac{1}{2}\sum_{i=1}^{n}\left(\mathbf{u}_i^T - \mathbf{u}_{i-1}^T\right)\left(\Delta\hat{\mathbf{f}}_i + \Delta\hat{\mathbf{f}}_{i-1}\right)\right]. \tag{13}$$

From (5), the change in the internal force due to removing or adding an element can be calculated as

$$\Delta\hat{\mathbf{f}} = \Delta x_e \mathbf{C}_e^T \mathbf{p}_e \tag{14}$$

which can be substituted into (13) to yield

$$\Delta E_p \approx \Delta x_e \lim_{n\to\infty}\left[\frac{1}{2}\sum_{i=1}^{n}\left(\mathbf{u}_i^T - \mathbf{u}_{i-1}^T\right)\mathbf{C}_e^T\left((\mathbf{p}_e)_i + (\mathbf{p}_e)_{i-1}\right)\right]. \tag{15}$$

Using the trapezoidal numerical integration method and noting the definition of the dissipated energy in (2), the above equation can be simplified as

$$\Delta E_p \approx \Delta x_e \lim_{n\to\infty} [(E_e)_i - (E_e)_{i-1}] = \Delta x_e E_e, \tag{16}$$

where $(E_e)_i$ is the total strain energy of the e-th element after i iteration through solving the nonlinear equilibrium; and E_e is the final strain energy of the e-th element upon completion of the loading cycle. Noting the definition of design variables from Section 2.2, one can observe that for removing an element $\Delta x_e = -1$ and for introducing an element $\Delta x_e = +1$.

Based on (16) we define the following sensitivity number for an element e

$$\alpha_e = \frac{\Delta E_P}{\Delta x_e} = E_e \tag{17}$$

which is a measure of efficiency of the e-th element. Note that the sensitivity numbers defined in (17) are always positive. Remembering that the maximum value of E_P is desirable and noting that $\Delta E_P = \alpha_e \Delta x_e$, for removing an element ($\Delta x_e = -1$), the element with the lowest sensitivity is the most suitable candidate for removal. On the other hand, introducing a new element strengthens the adjacent elements and results in $\Delta x_e > 0$. Hence, in this case, the new element should be added in the neighborhood of the elements with higher sensitivity numbers.

2.4. Shape restrictions

BESO is naturally a topology optimization method which can introduce new holes and fill the current holes in the domain. To prevent the algorithm from changing the topology of the domain and restrict it to shape optimization, it is necessary to restrict the designable domain to the elements at the boundary of the

slits. In other words, the elements are only allowed to be removed from and added to the boundary line. The designable domain in each iteration is thus redefined as

$$\mathcal{D} = \{e | \exists i, j \in \mathcal{B} : i, j \in e \wedge i \neq j\}, \tag{18}$$

where $\mathcal{B}$ is the set of boundary nodes defined as

$$\mathcal{B} = \{j | \exists e_m \in \mathcal{M}, e_v \in \mathcal{V} : j \in e_m \cap e_v\} \tag{19}$$

with $\mathcal{M}$ and $\mathcal{V}$ representing the sets of solid and void elements.

2.4.1. Periodicity

In order to enhance the manufacturability of the solutions, a periodic cellular design is considered with four identical cells similar to the initial SSD design. The BESO method has been previously proved useful in producing optimal periodic structures [22]. To deal with periodic design problems, the design domain should be divided into a number of identical cells. The sensitivity numbers of corresponding elements in all of these cells are then averaged and this averaged value is used as the sensitivity number for all of these elements. This procedure can be illustrated as

$$\alpha_i = \frac{1}{N_{cell}} \sum_{j=1}^{N_{cell}} \alpha_{i,j}, \tag{20}$$

where α_i is the averaged sensitivity number of the i-th element in all cells; $\alpha_{i,j}$ is the (original) sensitivity number of the i-th element in the j-th cell; and N_{cell} is the number of cells. In this manner, the BESO algorithm treats all the cells identically and maintains the periodicity of the design.

2.4.2. Mirroring

Because of the non-linear nature of the problem, the loading sequence will affect the mechanical responses. This will generally result in an unsymmetrical

optimal shape. Hence one would get mirrored shape results if once considers a displacement cycle starting with an upward moving (↑↓↑) and once with an initial downward moving (↓↑↓). In real case, however, it is uncertain which direction is more likely to happen. It is thus reasonable to consider both of these loading cases. To do so, one should consider the mechanical responses of the two load cases and add them up together to obtain the correct sensitivity number. However, as the loading sequences are just mirror reflections of each other, we just need to add the sensitivities of mirrored elements together. This can be mathematically expressed as

$$\bar{a}_i = a_i + a_{\overset{\leftrightarrow}{i}} \tag{21}$$

where $\bar{a}_i$ is the corrected (mirrored) sensitivity number of the i-th element; and $\overset{\leftrightarrow}{i}$ is the element at the same location as the i-th element in the mirrored structure.

2.5. BESO procedure

As already mentioned in Section 2.3, the elements with the lowest sensitivity numbers are the least efficient and should be removed while the ones with highest sensitivity numbers are the most efficient and should be strengthened. In the BESO procedure strengthening the elements is via introducing new elements in their vicinity. In the new BESO algorithm [14], a filtering scheme is used to assign a sensitivity number to the void elements in the vicinity of solid elements. The filtering scheme is a wighted averaging which can be expressed as

$$\hat{\alpha}_i = \frac{\sum_{j=1}^{N} \bar{\alpha}_j w_{ij}}{\sum_{j=1}^{N} w_{ij}}, \tag{22}$$

where $\hat{\alpha}_i$ is the filtered sensitivity number of the i-th element and w_{ij} is a linear weighting factor defined as

$$w_{ij} = \min\{0, R - d_{ij}\}. \tag{23}$$

Here R is a positive scalar value known as filtering radius and d_{ij} is the distance between the centroids of the i-th and j-th elements.

Using this filtering scheme, the void elements in the neighborhood of the elements with higher sensitivity number will obtain higher filtered sensitivity numbers. Hence, in the BESO procedure, the void elements with the highest filtered sensitivity numbers can be assumed as the most efficient choices for introduction to the system. This filtering scheme also smooths the jagged boundary lines and overcomes some numerical instabilities such as checkerboard formation [23].

2.5.1. Adding and removing elements

In the optimization problem (1), the volume is fixed to a predefined value, $\bar{V}$. Starting from a feasible design with $V = \bar{V}$, one needs to add and remove a same amount of material to keep the volume unchanged. Using identical elements to discretize the designable domain, the number of adding and removing elements should be equal. If a solid element has a lower sensitivity number than a void element, the two elements should be switched. However, in order to prevent sudden changes, the maximum number of changes should be restricted. The limiting number of changes is referred to as 'move limit' hereafter and is denoted by m. Comparing with the BESO algorithm proposed by Huang and Xie [14], the move limit used here is equivalent to the maximum adding ratio, i.e. $m = AR_{max}$.

The optimization loop continues until the following condition is met

$$\frac{\sum_{i=1}^{l} E_P^{(k-i+1)} - E_P^{(k-i)}}{\sum_{i=1}^{l} E_P^{(k-i+1)}} < \tau, \tag{24}$$

where $E_P^{(i)}$ denotes the value of the objective function at i-th iteration; k is the current iteration number; τ is the convergence tolerance selected as 10^{-4} here; and l is chosen as 5 in the numerical tests.

2.6. Numerical results

The initial design is depicted in Fig. 3. A series of tests are conducted with different material volumes. Table 1 summarizes the test cases and their specifications.

Table 1: The specifications of test cases.

Case name	Slot opening w (Fig. 3) (mm)	Volume fraction (%)	Number of elements $N = 4N_{cell}$
V84	5	85.6	7360
V76	7.5	78.4	6720
V68	10	71.2	6080
V60	12.5	64.0	5440

In all cases the volume is kept constant so that the objective function values for different iterations could be compared. The move limit is chosen as $m = 0.005N$. The number of elements, N, for each case is reported in Table 1. This relatively small value is adopted due to the small number of elements in the design domain which is limited to the boundaries of the holes. The filtering radius is selected as 5mm through all the tests. The initial and final cell designs and the evolution of the objective functions (energy dissipation) for the test cases are illustrated in Fig. 4 to Fig. 7.

The increasing trend of the energy dissipation through optimization iterations, which can be observed in all cases, verifies the proposed approach. It can be seen that in all cases, the energy dissipation increases significantly. In these four cases, the energy absorption capacity of the optimum results are improved 58 to

96% compared to the energy dissipation capability of the initial designs. Table 2 summarizes the improvements in the energy absorption capacity of the test cases.

In order to achieve a simple manufacturable shape, some shape restrictions have been enforced to the shape optimization problem. Restricting the designable domain to the small set $\mathcal{D}$ defined in (18) to maintain the topology, forcing the design to be periodic, and mirroring will all impose limitations to the optimization process by making its feasible space smaller. Furthermore because of the binary nature of the BESO algorithm, the feasible space in not continuous. This restricted, discrete feasible space causes some oscillations in the objective function values observable at the end of the optimization procedures, when the solution is going to converge.

In all cases the optimum cell design is tapered in the middle. As these four cases had different material volume, it can be concluded that for this sort of dampers the diamond shaped holes provide the best energy dissipation capacity irrespective of the material volume.

Table 2: The improvement of the energy dissipation of the test cases after optimization.

	E_P (J)		
Case name	Initial	Final	Improvement (%)
V84	1124.	2203.	96
V76	863.	1440.	67
V68	631.	1000.	58
V60	436.	717.	64

2.7. Postprocessing

In order to remove the jagged boundaries of the resulted shapes and reduce the stress concentration it is necessary to smooth the boundaries of the resulted shapes. A postprocessor is written to automatically smooth the boundaries of the optimal shapes using Bézier curves. Fig. 8 shows the smoothed results. It can be seen that irrespective of the volume fraction, all the optimum shapes include diamond shaped holes.

To check the effect of the shape optimization on stress distribution, the smoothed optimal shape of the case V60 is tested against its smoothed initial shape. The force-displacement curve and the stress distribution of the initial and optimal shapes are depicted in Fig. 9 and Fig. 10 respectively.

It can be seen in Fig. 9 that the optimum shape provides a stiffer design compared to the initial shape. After undergoing 10mm of displacement, the initial shape produces a reaction of 16.4kN while the reaction generated in the optimal shape is 24.3kN. Also a comparison between the stress levels in Fig. 10 reveals that the optimal shape provide a much evener stress distribution. The stress concentration zones in the corner of the holes visible in the initial design are eliminated in the optimal shape. The stress concentration zones are prone to fatigue and undesirable brittle failure under cyclic loads. The fatigue failure of the SSD devices at these zones have been reported in Chan and Albermani [18].

2.8. Optimal design

Based on the shape optimization results and Fig. 8, three specimens with the shape design depicted in Fig. 11 are fabricated. These specimens are used for experimental tests as discussed in the following sections. Because of the tapered shape we refer to this design as TSSD.

3. Experimental verification

The objective of the experiments is to verify the cyclic characteristics of the optimized shape. Furthermore, strength-degradation and low-cycle fatigue characteristics of the device are not predicted by the current finite element model. They must be investigated by physical experiment.

3.1. Test setup, instrumentation and loading history

Identical setup with previous tests [18] was used such that comparable results could be obtained. The test setup is shown in Fig. 12. The specimens were installed between a ground beam and an L-beam, securely fastened by four M16 bolts (snug tight) on each side. Forced displacement was applied by an MTS 100kN capacity computer-controlled actuator quasi-statically to the specimen via the L-beam. To ensure the verticality of the applied load, a pantograph system was welded to the right hand side of the L-beam. The pantograph system also prevented the L-beam from deflecting out-of-plane. The complete test setup rested on a reaction frame which was significantly stiffer. The centerline of the actuator implied an eccentricity to the specimen, measured 162mm to the centerline of the specimen. A free-run of the setup (i.e. without the specimen installed) was performed and the result showed that friction and the effect of gravity were considered negligible. The setup was robust and repeatable, no visible damage occurred after all tests were carried out. Fig. 13 shows a photograph of the setup with specimen installed.

Displacements of the specimens were measured independently by a pair of LVDTs, marked as 1 and 2 in Fig. 12. While LVDT 1 measures the elastic deformation of the support, the difference across LVDT 1 and 2 measured the absolute

Table 3: Specimens and test results.

Specimen	Test history	P_y (kN)	δ_y (mm)	k_d ($\frac{\text{kN}}{\text{mm}}$)	P_{max} (kN)	P_{min} (kN)	N_c	E_d (kJ)
TSSD-1	0.5, 1.0, 1.5, 2.5, 5.0, 7.5, 10.0, 12.5, 15.0, 20.0 and 25mm	9.1	1.8	4.22	15.9	-11.5	33 [a]	8.23
TSSD-2	Constant amplitude at 20mm	9.8	2.7	4.18	15.5	-11.1	15	7.74
TSSD-3	Constant amplitude at 12.5mm	9.9	2.8	4.55	15.1	-12.0	37	12.31

[a] Note: TSSD-1 did not break after 33 cycles were completed.

distortion of the test specimen.

Specimen TSSD-1 was tested under identical displacement history with previously study on SSD [18]. The load history comprised three repeated cycles at amplitudes of 0.5, 1.0, 1.5, 2.5, 5.0, 7.5, 10.0, 12.5, 15.0, 20.0 and 25mm. TSSD-2 and TSSD-3 were tested under a constant displacement until complete breakage of the specimens. Table 3 summarizes the test histories and key results.

3.2. Specimens

Based on the result of optimization, three specimens were fabricated. Dimensions are shown in Fig. 11. All specimens (each 100mm long) in this study were cut from the same structural wide-flange section $152 \times 152 \times 37$ Universal Column to BS4449 (depth $\times$ flange width $\times$ web thickness $\times$ flange thickness is $161.8 \times 152.2 \times 8 \times 11.5$mm respectively). Consequently, the web thickness t

is identical and material strengths of all specimens may be assumed equal. Four 16mm diameter holes were drilled on each flange for connection to the test rig. Two standard test coupons were taken from the web of the section. Coupon tests gave an average tensile yield stress of 316.5N/mm^2 and an average Modulus of Elasticity of 206.1kN/mm^2.

3.3. Test results and discussion

All three specimens deformed in a stable manner under the cyclic tests. The strips deformed in double curvature as expected. Fig. 14(a) to (c) present the force-displacement hysteresis obtained from the cyclic tests. A positive sign refers to downward force and displacement. Shear strain γ (i.e. distortion divided by total width of device) of the specimens are also shown. Positive yield strength P_y, its corresponding yield displacement δ_y, elastic stiffness k_d, positive peak strength P_{max}, negative peak strength P_{min}, the number of cycles to failure N_c and energy dissipation E_d are tabulated in Table 3.

It is clear that all specimens have yielded at small displacement and exhibited very stable hysteretic behavior with a gradual transition between the elastic and inelastic regime. The specimen response magnitude was slightly lesser than the input displacement history due to elastic deformation of the support. Absolute displacements (difference across LVDT 1 and 2) are used to determine the mechanical properties of the specimens. The connection of the specimens by four structural bolts on each flange performed satisfactory; no significant distortion was observed after the tests. Fig. 15 shows the damaged specimen TSSD-1 after testing.

3.4. Specimen TSSD-1

TSSD-1 completed all cycles without breakage. At the end of the 25mm cycle, force was released such that the specimen was left deformed. A photograph of the specimen after all cycles is shown in Fig. 15. Its force-displacement hysteresis is shown in Fig. 14(a). Very stable hysteresis without noticeable sign of strength deterioration was observed. Cracks have developed on the bar surfaces due to repeated loading, but they did not cause breakage. Initial yield strength and displacement were recorded at 9.1kN and 1.8mm respectively. Bauschinger effect was apparent, with negative peak strength only 72% of the positive peak.

TSSD-1 dissipated 8.23kJ at the end of the cycles. Energy dissipation of TSSD-1 is shown in Fig. 16. Result from specimen SL-1 [18] is plotted on the same chart for comparison. To account for different volume of steel involved in specimens, energy is expressed as energy dissipated per unit volume of steel. Here the volume of steel between fillets is taken into consideration as the flange does not contribute to energy dissipation. There is a 37% increase in energy dissipation and it is evident that the optimization process has resulted in a more efficient design. From the same diagram it is clear that, after optimization, TSSD-1 sustained a much larger cumulative displacement compared to SL-1. The enhanced resistance against low-cycle fatigue is clear.

3.5. Specimens TSSD-2 and TSSD-3

TSSD-2 and TSSD-3 were fabricated to identical dimensions as TSSD-1, but these two specimens were tested under constant amplitudes until complete breakage. They enable us to identify their energy dissipating capacity under different displacement amplitudes. TSSD-2 was tested at 20mm ($\mu \approx 11$) while TSSD-3 was tested at 12.5mm ($\mu \approx 7$). Their load-displacement hysteresis are shown

in Fig. 14(b) and (c). Both specimens exhibited stable behavior without noticeable degradation during their early cycles. TSSD-2 sustained 15 complete cycles prior to failure, while TSSD-3 sustained 37 cycles. TSSD-2 dissipated 7.74kJ of energy, while TSSD-3 dissipated 12.31kJ. It is interesting that at relatively low displacements, the device dissipated a much larger amount of energy.

4. Conclusion

This paper proposed a new steel slit damper design, TSSD, based on the numerical shape optimization results. A previously proposed steel slit damper, SSD, with straight uniform slit width has been taken as the initial design. An optimization procedure has been proposed based on the well-known BESO method to find the optimum shape of the slits. Some shape restrictions have been introduced and imposed in the optimization procedure to maintain the topology of the design and restrict it to a symmetric periodic cellular shape with 4 cells. The plastic energy dissipation of the damper after one cycle of displacement loading with 10mm amplitude has been taken as the objective function. The optimization problem has been then stated as maximizing the objective function while the material volume is kept constant and the shape is restricted. Four initial models with similar shape to SSD has been considered as the initial designs each having a different material volume. The resulted evolution of the objective function values for all the cases has shown a significant increase in the energy dissipation capacity verifying the proposed optimization procedure. Improvements of 58 to 96% in the energy absorption capacity of the designs have been recorded. The optimum shapes were all include bars tapered in the middle forming diamond shaped slits irrespective of the material volume.

A postprocessor has been used to smooth the optimum results using Bézier curves. It has been demonstrated that the optimum tapered slit design provides an even stress distribution and the stress concentration noticeable in the initial straight slit design has been eliminated in the optimum design. This even stress distribution can significantly improve the behavior of the damper under fatigue.

The finite element model used in the optimization process was not capable of predicting failure and fatigue of the design. Therefore, based on the optimization findings, three TSSD specimens were fabricated and put under cyclic tests. Under identical test setup and load history, the TSSD specimen dissipated 37% more energy per unit volume compared to the previously tested SSD, and significantly delayed low-cycle fatigue. It should be noted that this figure is not comparable with the improvements reported on Table 2 because the volume of the original SSD and the proposed TSSD are not equal. Experiments confirmed that the optimization process is robust and it is suitable for future development of energy dissipaters.

Acknowledgement

Experimental works described in this paper is carried out during an academic visit to City University of Hong Kong by the second author, supported by the Research Grant Council of Hong Kong City University RGC 115208.

References

[1] Soong TT, Spencer Jr BF. Supplemental energy dissipation: state-of-the-art and state-of-the-practice. Eng Struct 2002;24(3):243–59.

[2] Bergman DM, Goel SC. Evaluation of cyclic testing of steel-plate devices for added damping and stiffness. Tech. Rep. UMCE 87-10; Department of Civil Engineering, University of Michigan; Ann Arbor, Michigan; 1987.

[3] Tsai KC, Chen HW, Hong CP, Su YF. Design of steel triangular plate energy absorbers for seismic-resistant construction. Earthq Spectra 1993;9(1993):505–28.

[4] Chan RW, Albermani F, Williams MS. Evaluation of yielding shear panel device for passive energy dissipation. J Constr Steel Res 2009;65(2):260–8.

[5] Black CJ, Makris N, Aiken ID. Component testing, seismic evaluation and characterization of buckling-restrained braces. ASCE J Struct Eng 2004;130(6):880–94.

[6] Koetaka Y, Chusilp P, Zhang Z, Ando M, Suita K, Inoue K, et al. Mechanical property of beam-to-column moment connection with hysteretic dampers for column weak axis. Eng Struct 2005;27(1):109–17.

[7] ASCE/SEI 7-05. Minimum Design Loads for Buildings and Other Structures. ASCE Publications; 2006.

[8] Bendsøe MP, Sigmund O. Topology Optimization - Theory, Methods, and Applications. Berlin: Springer; 2003.

[9] Xie YM, Steven GP. Evolutionary structural optimization. London: Springer; 1997.

[10] Xie YM, Steven GP. A simple evolutionary procedure for structural optimization. Comput Struct 1993;49(5):885–96.

[11] Querin OM, Steven GP, Xie YM. Evolutionary structural optimisation (eso) using a bidirectional algorithm. Engineering Computations 1998;15(8):1031–48.

[12] Querin OM, Young V, Steven GP, Xie YM. Computational efficiency and validation of bi-directional evolutionary structural optimisation. Comput Method Appl Mech Eng 2000;189(2):559–73.

[13] Yang XY, Xie YM, Steven GP, Querin OM. Bidirectional evolutionary method for stiffness optimization. AIAA J 1999;37(11):1483–8.

[14] Huang X, Xie YM. Convergent and mesh-independent solutions for the bi-directional evolutionary structural optimization method. Finite Elem Anal Des 2007;43(14):1039–49.

[15] Huang X, Xie YM, Lu G. Topology optimization of energy-absorbing structures. Int J Crashworthiness 2007;12(6):663–75.

[16] Huang X, Xie YM. Topology optimization of nonlinear structures under displacement loading. Eng Struct 2008;30(7):2057–68.

[17] Ghabraie K. Exploring topology and shape optimisation techniques in underground excavations. Phd thesis; RMIT University; Melbourne, Australia; 2009.

[18] Chan RW, Albermani F. Experimental study of steel slit damper for passive energy dissipation. Eng Struct 2008;30(4):1058–66.

[19] Rozvany GI, Querin OM, Gaspar Z, Pomezanski V. Extended optimality in topology design. Struct Multidiscip Optim 2002;24(3):254–61.

[20] Buhl T, Pedersen C, Sigmund O. Stiffness design of geometrically nonlinear structures using topology optimization. Struct Multidiscip Optim 2000;19(2):1615–488.

[21] Jung D, Gea HC. Topology optimization of nonlinear structures. Finite Elem Anal Des 2004;40(4):1417–27.

[22] Huang X, Xie YM. Optimal design of periodic structures using evolutionary topology optimization. Struct Multidiscip Optim 2008;36(6):597–606.

[23] Sigmund O, Petersson J. Numerical instabilities in topology optimization: A survey on procedures dealing with checkerboards, mesh-dependencies and local minima. Struct Multidiscip Optim 1998;16(1):68–75.

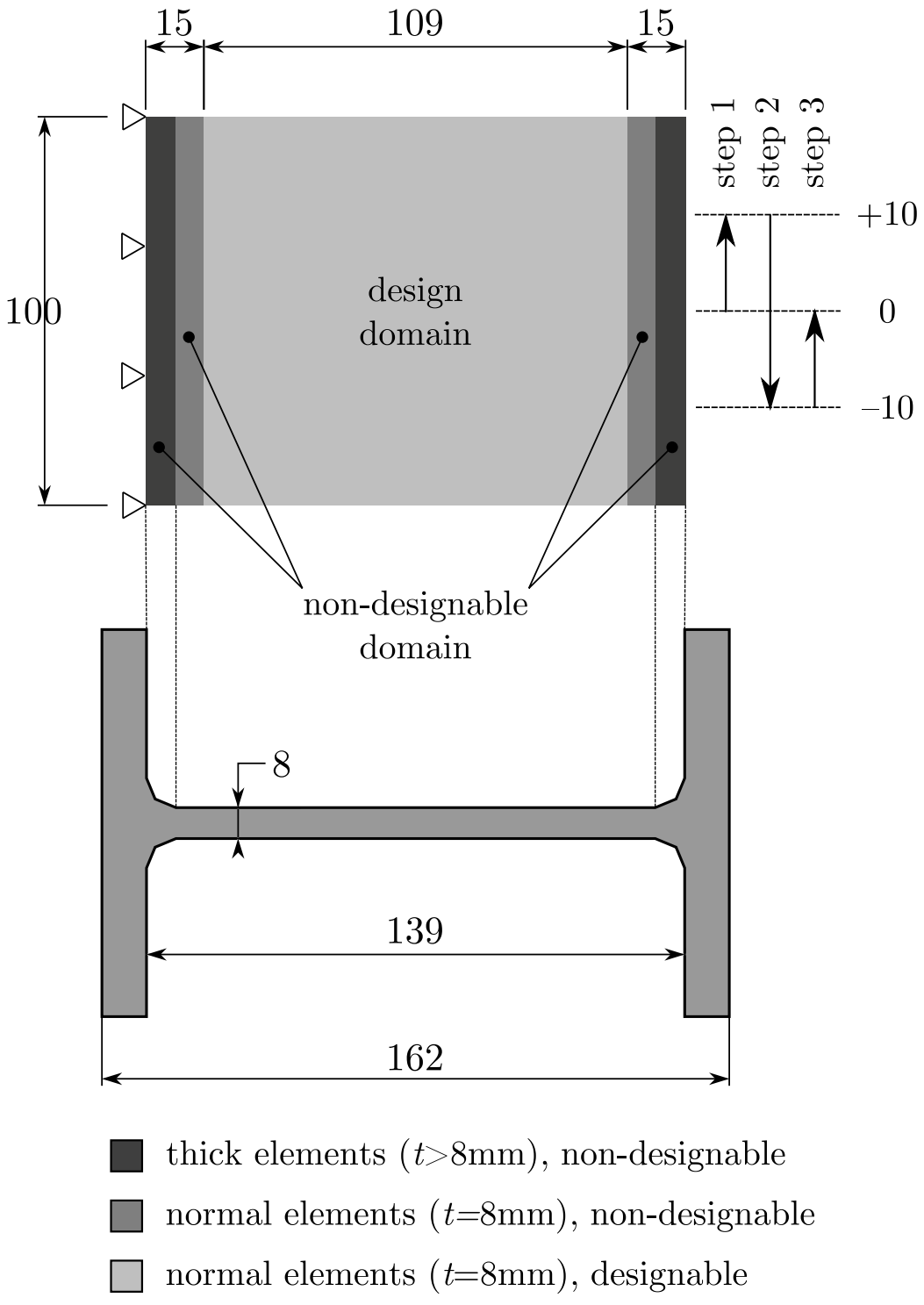

Figure 2: The designable and non-designable domains.

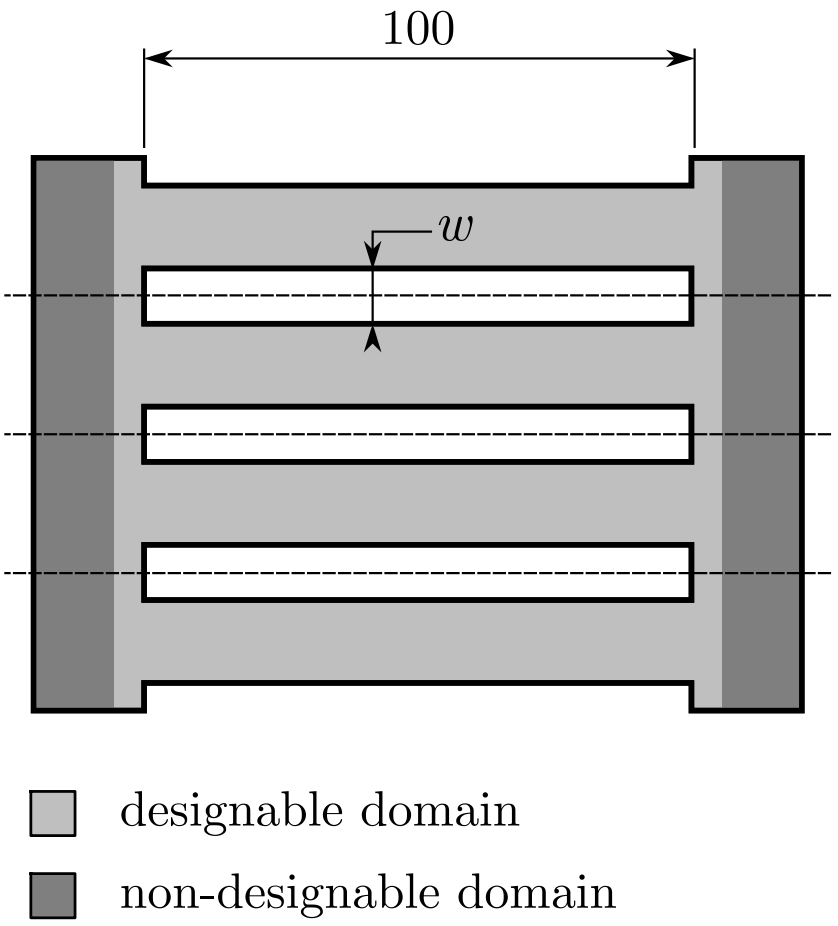

Figure 3: The initial design.

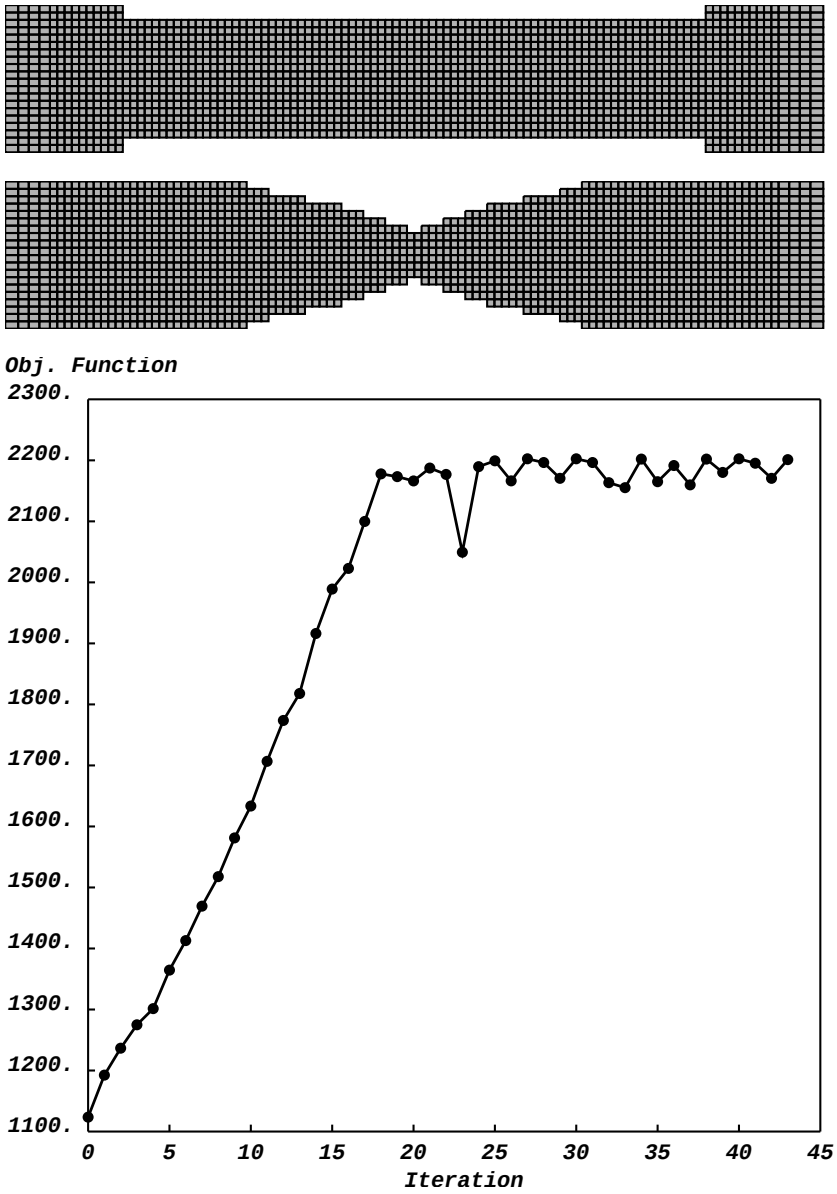

Figure 4: The results of case V84.

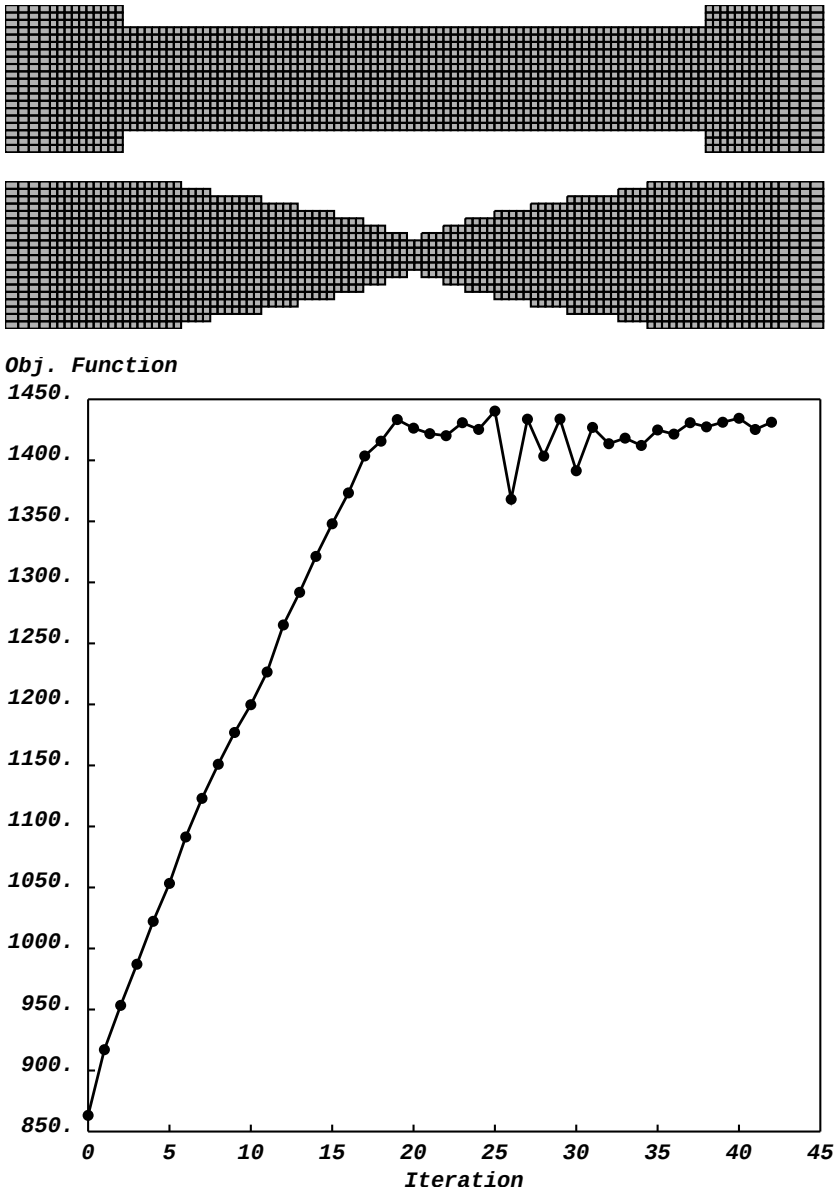

Figure 5: The results of case V76.

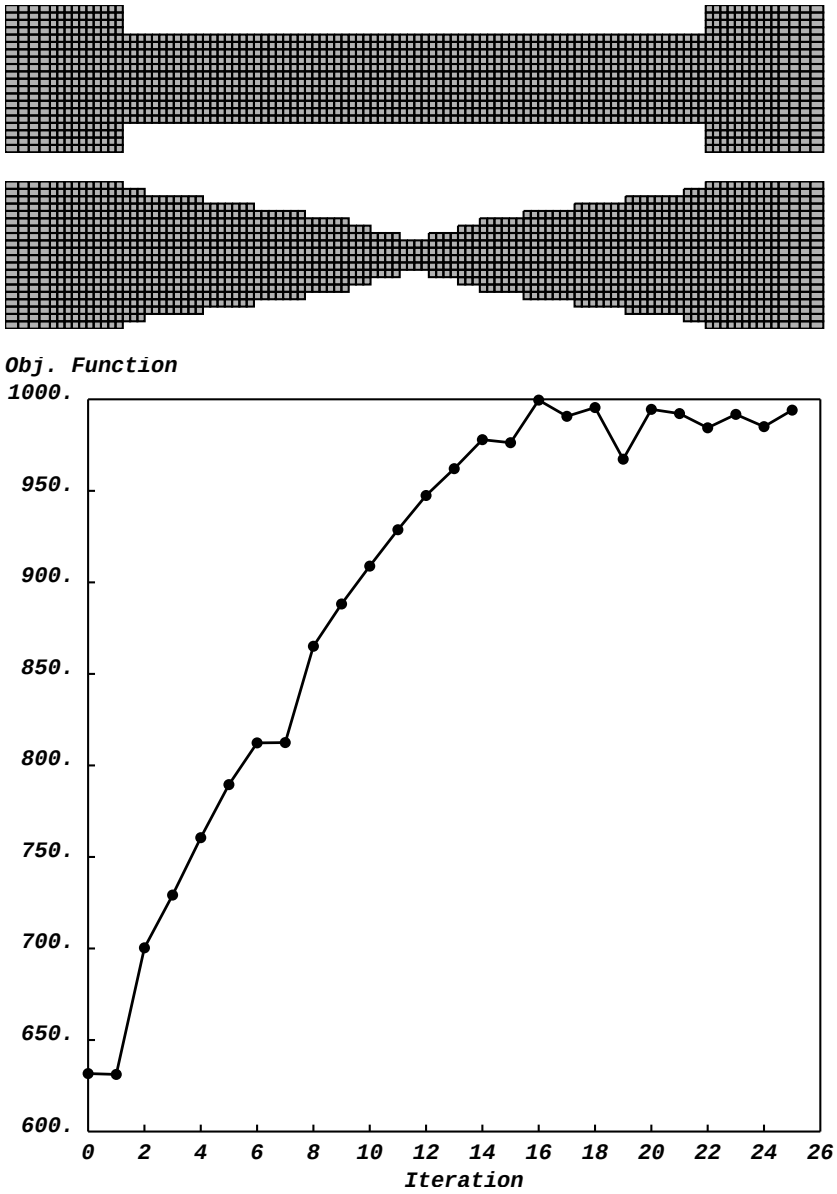

Figure 6: The results of case V68.

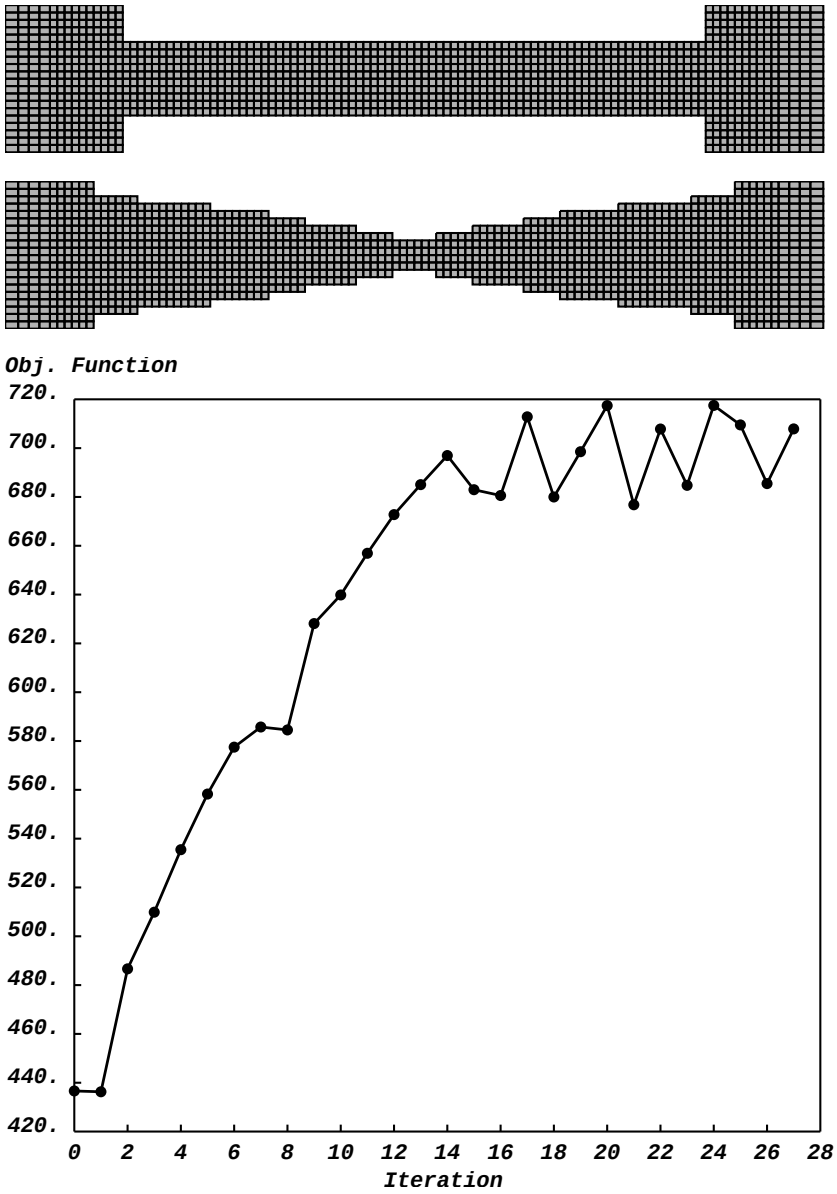

Figure 7: The results of case V60.

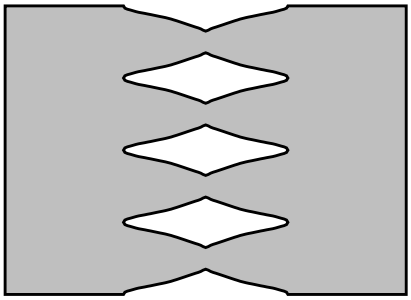

(a) Case V84

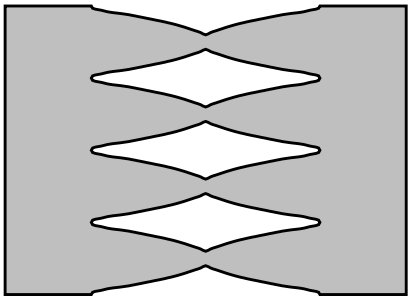

(b) Case V76

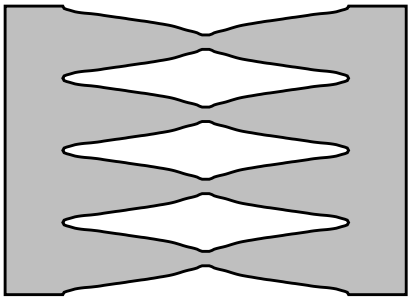

(c) Case V68

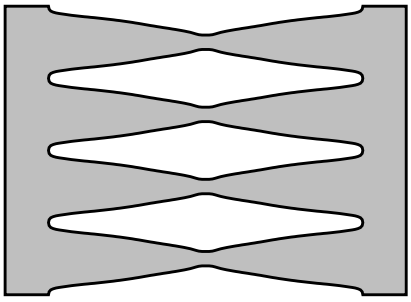

(d) Case V60

Figure 8: The smoothed results.

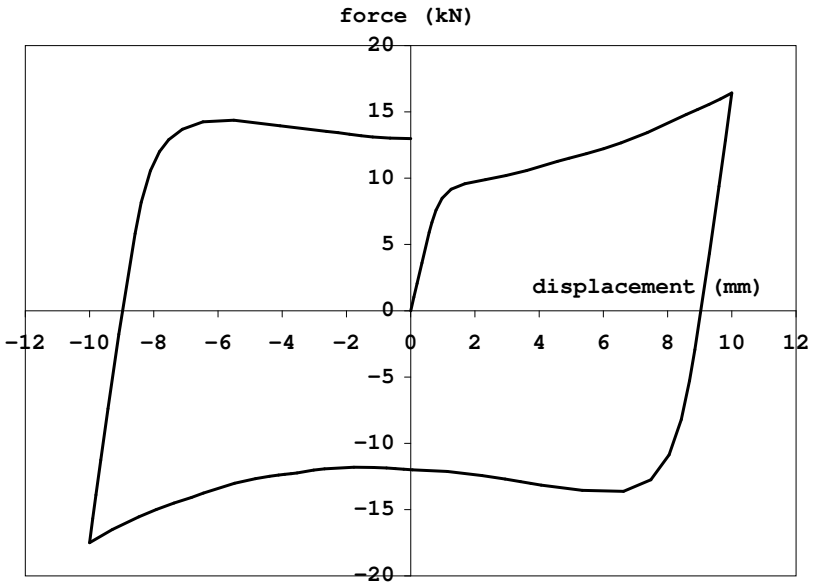

(a) initial design

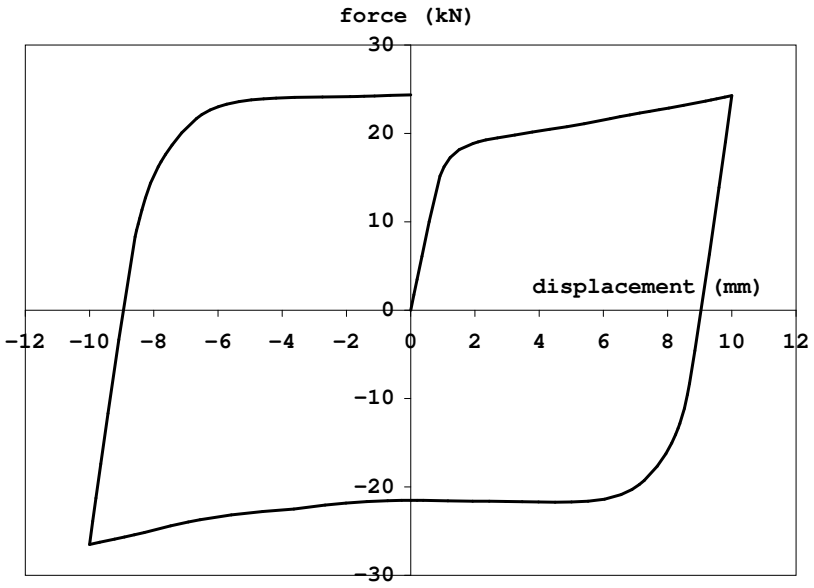

(b) optimal design

Figure 9: Comparing the force-displacement curves of the initial and optimal designs for case V60. The stress values are in MPa.

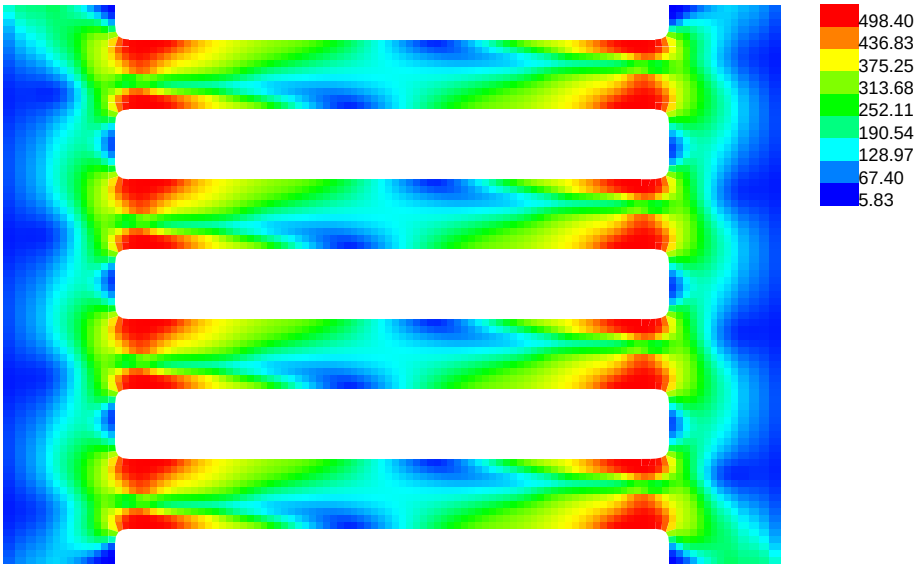

(a) initial design

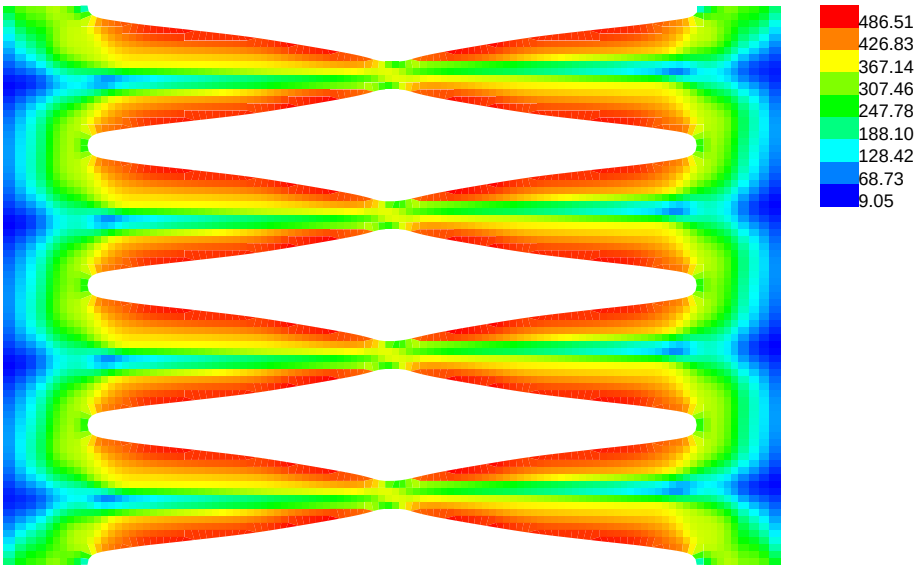

(b) optimal design

Figure 10: Comparing the stress distribution of the initial and optimal designs for case V60. The stress values are in MPa.

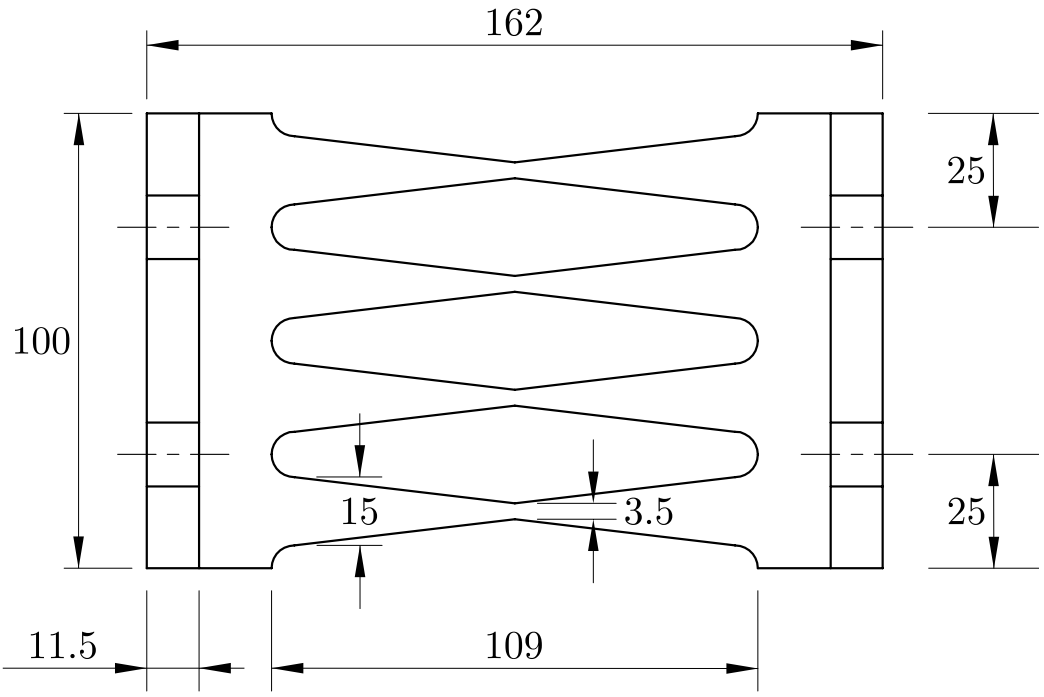

Figure 11: TSSD shape design used for experiments.

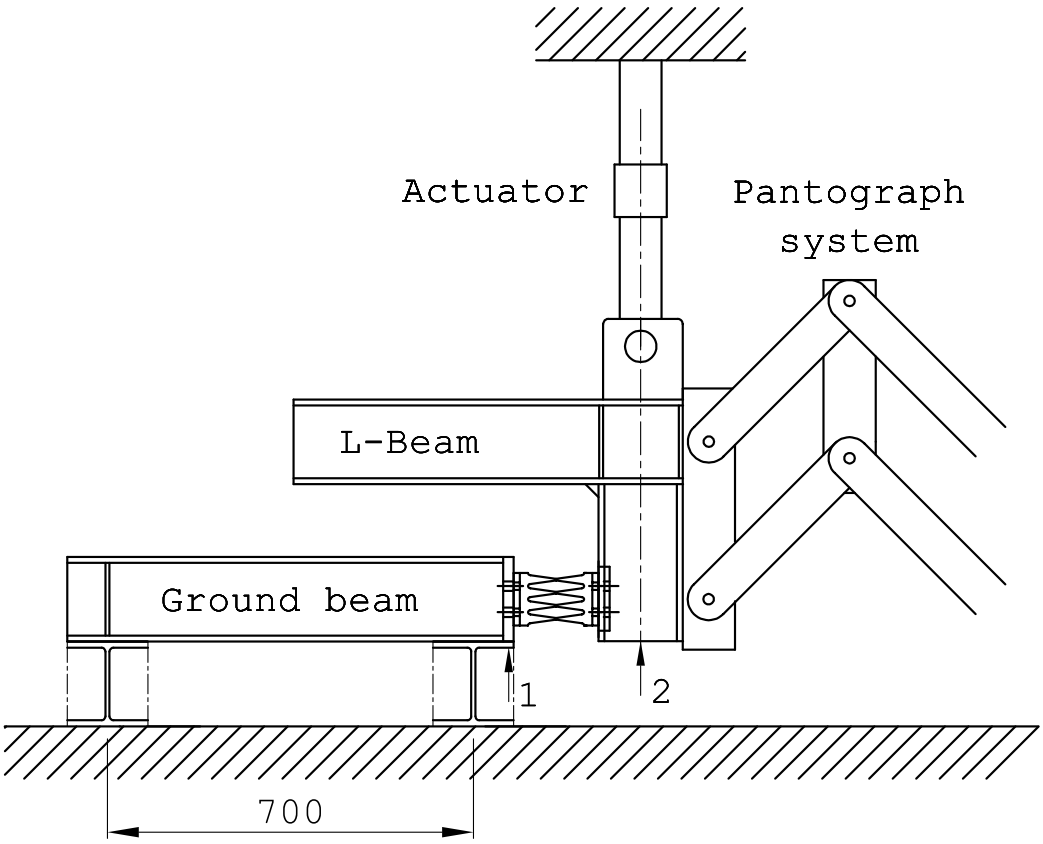

Figure 12: Test setup.

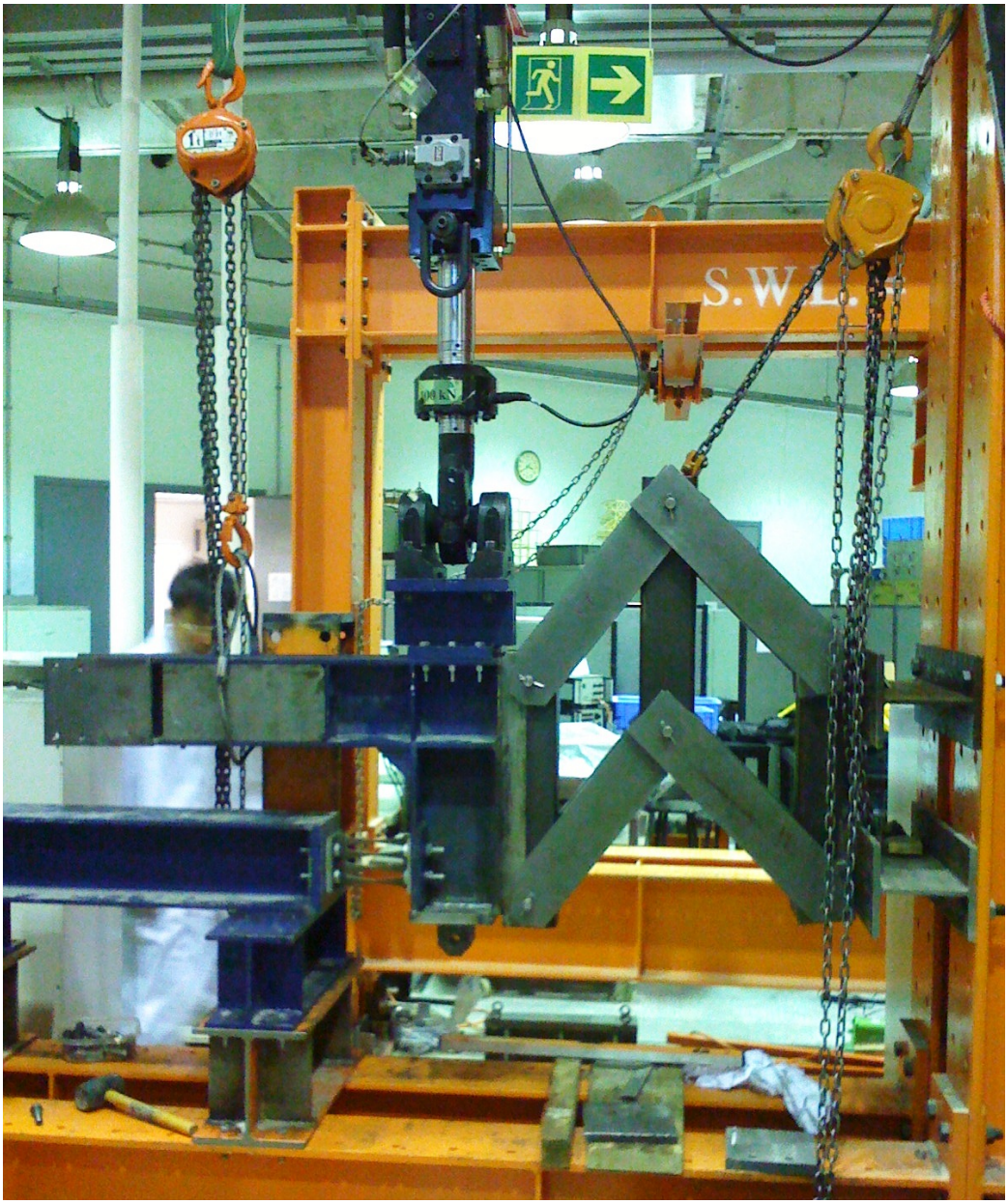

Figure 13: Overview of test setup.

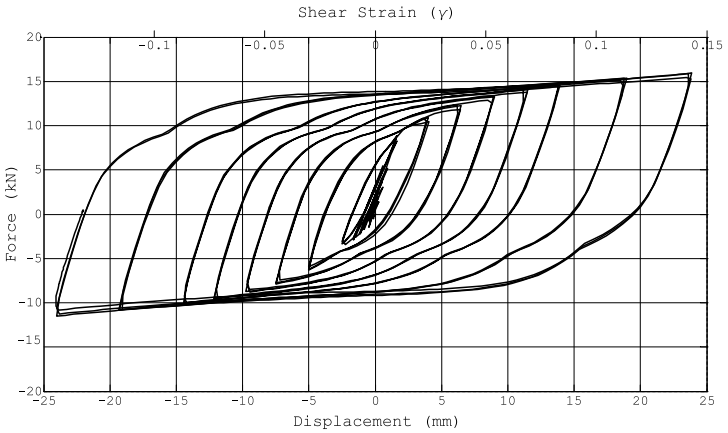

(a) TSSD-1

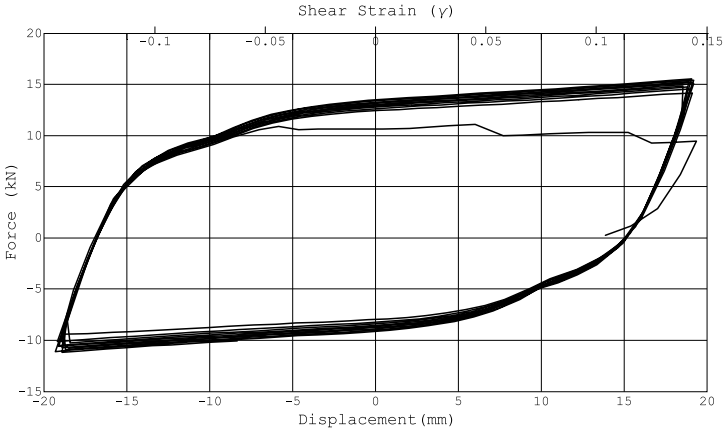

(b) TSSD-2

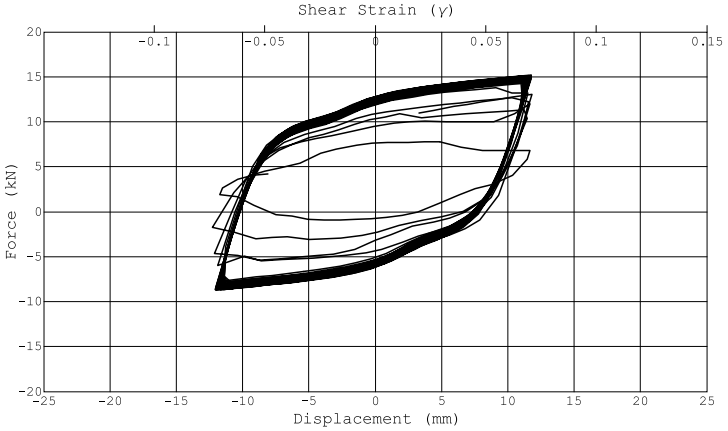

(c) TSSD-3

Figure 14: Force-displacement hysteresis of TSSD specimens.

Figure 15: Specimen TSSD-1 after the test.

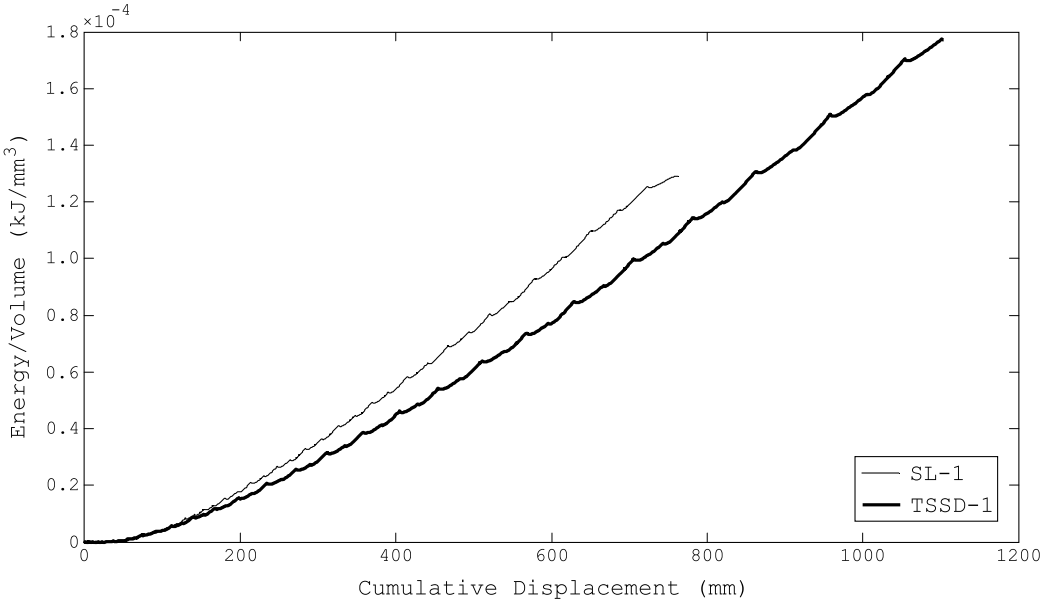

Figure 16: Cumulative energy dissipation.